

Seismic Imaging of the Salt Lake Basin Using Joint Inversion of Receiver Functions and Rayleigh Wave Data



Key Points:

- We analyze receiver functions (RFs) from permanent seismic network stations and temporary seismic arrays in the Salt Lake basin
- We jointly invert RFs and Rayleigh wave ellipticities and phase velocities to obtain a new velocity model of the basin
- Our new velocity model reveals larger and sharper sediment thickness variations across the Wasatch fault zone compared to previous models

Supporting Information:

Supporting Information may be found in the online version of this article.

Correspondence to:

H. J. Kim,
hkim.geo@gmail.com;
hyejeong.kim@utah.edu

Citation:

Kim, H. J., Lin, F.-C., Pechmann, J. C., Hardwick, C. L., & McKean, A. P. (2025). Seismic imaging of the Salt Lake basin using joint inversion of receiver functions and Rayleigh wave data. *Journal of Geophysical Research: Solid Earth*, 130, e2024JB030927. <https://doi.org/10.1029/2024JB030927>






Received 9 DEC 2024
 Accepted 14 MAR 2025

Author Contributions:

Conceptualization: HyeJeong Kim, Fan-Chi Lin, James C. Pechmann, Christian L. Hardwick, Adam P. McKean
Data curation: HyeJeong Kim, Fan-Chi Lin, Christian L. Hardwick
Formal analysis: HyeJeong Kim
Funding acquisition: Fan-Chi Lin, Christian L. Hardwick, Adam P. McKean
Investigation: HyeJeong Kim
Methodology: HyeJeong Kim
Project administration: Fan-Chi Lin, Christian L. Hardwick, Adam P. McKean
Resources: Fan-Chi Lin
Software: HyeJeong Kim

© 2025 The Author(s).

This is an open access article under the terms of the [Creative Commons Attribution-NonCommercial License](https://creativecommons.org/licenses/by-nc/4.0/), which permits use, distribution and reproduction in any medium, provided the original work is properly cited and is not used for commercial purposes.

HyeJeong Kim¹ , Fan-Chi Lin¹ , James C. Pechmann¹ , Christian L. Hardwick² , and Adam P. McKean² 

¹Department of Geology and Geophysics, University of Utah, Salt Lake City, UT, USA, ²Utah Geological Survey, Salt Lake City, UT, USA

Abstract This study presents a new velocity model for the Salt Lake basin (SLB) in Utah, determined using data from permanent and temporary seismic stations located on top of the basin in the Salt Lake Valley (SLV) and nearby. A three-dimensional (3D) velocity model for the SLB is needed for accurate predictions of future damaging earthquake ground shaking in the heavily urbanized SLV, including Salt Lake City. The SLB part of the Wasatch Front community velocity model (WFCVM) currently serves this purpose. However, the current WFCVM is based primarily on gravity and borehole data with relatively few seismic constraints below depths of 100 m. In this study we use the first peak of SLV receiver functions (RFs), which is sensitive to a strong impedance contrast at the base of a semi-consolidated sediment layer. We jointly invert the RF waveform with Rayleigh wave ellipticity (H/V) and phase velocity measurements using the Markov chain Monte Carlo approach. Our new velocity model shows a greater combined thickness of unconsolidated and semi-consolidated sediments, compared to the WFCVM, in the northeastern SLB between the west-dipping East Bench fault section of the Wasatch fault and the antithetic West Valley fault zone to the west. We show that the new seismic velocity model explains the gravity patterns in the valley. The new velocity model from this study provides a basis for revising the SLB model in the WFCVM.

Plain Language Summary The 2020 M_w 5.7 Magna earthquake in Salt Lake City, Utah, reminded residents that the Salt Lake Valley (SLV) region is prone to damaging earthquakes from the Wasatch fault and other faults. In seismically active regions, a three-dimensional seismic velocity model is important for predicting ground-shaking hazards. The current model for the SLV area was constructed primarily from gravity and shallow well data due to the limited amount of seismic data then available in the valley. Since 2018, multiple temporary geophone arrays have reduced gaps in seismic station coverage. The expanded data set enables us to revise existing velocity models using distant earthquakes recorded by SLV seismic stations. The new velocity model from this study shows thicker sediment deposits in the northeastern SLV between the active traces of the west-dipping Wasatch fault zone on the east and the east-dipping West Valley fault zone on the west. Predicted gravity variations using the new velocity models show patterns consistent with the observed gravity. Our new velocity model provides a basis for revising the SLV part of the velocity model used for ground motion predictions.

1. Introduction

A sedimentary basin filled with low-velocity material amplifies seismic ground motion due primarily to energy conservation, focusing effects, and the trapping of seismic energy within the basin caused by reflections and generation of surface waves at the basin boundaries. The presence of a sedimentary basin is particularly concerning for seismic hazard because a basin typically amplifies and prolongs earthquake ground shaking, especially at longer periods, thereby increasing the severity of the damage (e.g., Baena-Rivera et al., 2023; Day et al., 2008; Hartzell et al., 2000; Joyner, 2000; Kawase, 2003; Moschetti et al., 2021; Stephenson et al., 2000). Hence, an accurate three-dimensional (3D) velocity model of a sedimentary basin is important for predicting ground-shaking hazards from local earthquakes. In some regions, geoscientists have made collaborative efforts to build community velocity models (CVMs), which are 3D velocity models that integrate information from a variety of geophysical and geologic studies (e.g., Boyd et al., 2024; Hirakawa & Aagaard, 2022; Magistrale et al., 2000).

In the Wasatch Front region of Utah, a Wasatch Front community velocity model (WFCVM; Magistrale et al., 2008) was developed to help address the ground-shaking hazard arising from the high probability of a

Supervision: Fan-Chi Lin, James C. Pechmann
Validation: HyeJeong Kim
Visualization: HyeJeong Kim
Writing – original draft: HyeJeong Kim, Fan-Chi Lin, James C. Pechmann
Writing – review & editing: HyeJeong Kim, Fan-Chi Lin, James C. Pechmann, Christian L. Hardwick, Adam P. McKeon

damaging earthquake on the active Wasatch fault zone (WF) (Petersen et al., 2024; Wong et al., 2016). The Salt Lake basin (SLB) contains layers of unconsolidated alluvial and lacustrine deposits, which are known from observations (Moschetti et al., 2021; Pankow & Pechmann, 2005; Williams et al., 1993) and numerical simulations (Hill et al., 1990; Roten et al., 2011, 2012; Wang et al., 2017) to exhibit site amplification effects. Simulated spectral accelerations at 2-s and 3-s period show positive correlations to depths to shear-wave velocity (V_S) isosurfaces, which are indicators of basin depth (Wang et al., 2017). Overall, the seismic velocities and the depths of velocity discontinuities are crucial elements of the SLB model.

In the WFCVM, there are three characteristic seismic discontinuities at depth, which are the R1, R2, and R3 discontinuities defined by Hill et al. (1990). R1 is interpreted as the boundary between unconsolidated Quaternary and semi-consolidated Tertiary sediments. R2 is interpreted as the boundary between the semi-consolidated Tertiary sediments and Tertiary consolidated sediments (sedimentary rock), and R3 is interpreted as the boundary between the Tertiary consolidated sediments and the basement rock. The largest seismic impedance contrast is at the R2 boundary (Hill et al., 1990; Pechmann et al., 2010). Throughout this study, we consider the depth to bedrock to be the depth of the R2 discontinuity. Numerical simulations show that R2 and, to a lesser extent, R1 act to trap seismic energy in the SLB, which contributes significantly to amplification and increased duration of ground shaking in the Salt Lake Valley (SLV) (Hill et al., 1990; Olsen et al., 1996).

The WFCVM was created by combining information on crustal velocities and thickness, basin velocities, and basin depths from various studies (Magistrale et al., 2008). The depth to bedrock in the SLB, that is, the interface between the semi-consolidated and consolidated sediments (R2), was modified from a model that Radkins (1990) obtained from a 3D inversion of gravity data with constraints from well reports and a few seismic reflection lines. Most of his constraints are located near the edges of the SLB, where the basin sediments are relatively thin. Magistrale et al. (2008) modified the Radkins (1990) R2 model by adding an offset along the Wasatch fault, assuming the subsurface fault geometry proposed by Bruhn et al. (1992). Basin gravity modeling involves starting with the complete Bouguer gravity anomaly (CBGA) and then separating the long-wavelength regional gravity field from the short-wavelength local gravity field resulting in a final residual gravity field. The residual gravity is directly related to the density and thickness of the sedimentary layers, with lower gravity values indicating a thicker sediment layer and vice versa. After the gravity inversion in Radkins (1990), the gravity data for the SLV has been improved by the addition of new measurements (Kleber et al., 2020; Smith et al., 2023).

The 2020 moment magnitude (M_w) 5.7 Magna, Utah, earthquake (Hiscock et al., 2023; Pang et al., 2020), recorded by the permanent network of the University of Utah Seismograph Stations (UUSS), has provided the best opportunity to date to evaluate the WFCVM, as it was the first $M_w > 5$ earthquake to occur near or in the SLB after the construction of the model. Ratios between synthetic and observed peak ground motions for this earthquake show that the synthetics underpredict the ground motions east of the epicenter, in the area between the West Valley fault zone (WVVFZ) on the west and the East Bench and Warm Springs faults (East Bench fault (EBF) and Warm Springs fault, respectively) on the east (Hutchings, 2023). These observations suggest the need for some improvement in the WFCVM.

Since the current version of the WFCVM was released in 2014, various efforts have been made to improve the velocity model for the SLB. For example, new measurements of average shear-wave velocity in the top 30 m (V_{S30}) have been derived from active source seismic data (Liberty et al., 2021). There has also been an extensive increase in passive source seismic data acquired for seismic imaging at shallow depths in the SLB. Temporary deployments of short-period geophones (“nodals”) have provided short-period surface wave phase velocity measurements (e.g., Gkogkas et al., 2021; Zhang et al., 2019) and Rayleigh wave ellipticity (H/V) measurements (Zeng et al., 2022) to model seismic velocities over the depth range of a few hundred meters. Zeng et al.’s (2022) inversion of Rayleigh wave phase velocity and H/V measurements from a 2020 nodal array was the first seismic analysis to build a velocity model for the whole SLB. Depth slices of their velocity model showed some consistencies with the WFCVM but also some differences. However, R2 depths were not resolved in their study due to the insensitivity of surface waves to discontinuities.

In this study, we explore the potential of using teleseismic receiver function (RF) analysis to help constrain the depth of the R2 discontinuity. The RF method is effective in detecting seismic discontinuities, using the P-wave to S-wave conversion (i.e., the Ps phase) at the discontinuity. Teleseismic P waves have steeply incident ray paths in the upper crust. Hence, the first significant peak in the radial component is the Ps phase from the discontinuity, which is observed as an apparent delay of the first large radial component peak relative to that of the vertical

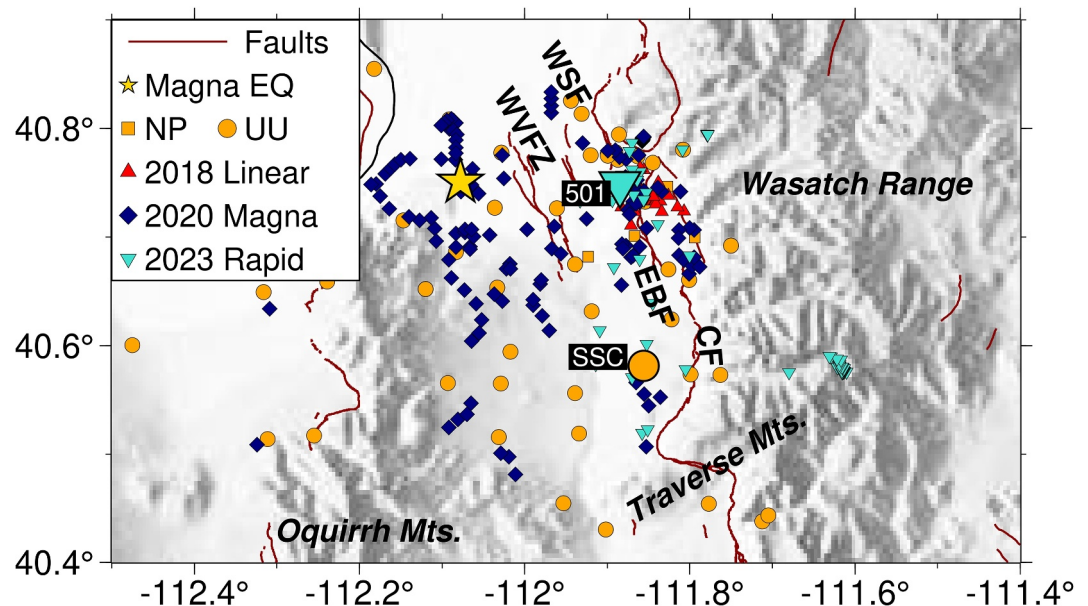


Figure 1. The distribution of stations in this study. Orange squares and circles, respectively, mark the stations of the permanent networks NP (U.S. Geological Survey, 1931) and UU (University of Utah, 1962). Red triangles mark the linear nodal array (shown in Figure 10a in detail) operated for one month in 2018 (2018 Linear; Lin & Kim, 2018), dark blue diamonds mark the nodal array that operated for the aftershock monitoring of the Magna earthquake for one month in 2020 (2020 Magna; Allam, 2020), and turquoise inverted triangles mark nodal stations that operated for a few months to a year in 2023–2024 (2023 Rapid; Zeng & Lin, 2023). The yellow star marks the epicenter of the 18 March 2020, M_w 5.7 Magna earthquake. The dark red lines show Quaternary fault traces (U.S. Geological Survey and Utah Geological Survey, 2019). Names of major faults are abbreviated as follows: WSF, Warm Springs fault; WVFZ, West Valley fault zone; EBF, East Bench fault, and CF, Cottonwood fault.

component. Some recent studies have used the Ps phase delay and/or higher order multiples for characterizing sediment thicknesses (e.g., Chichester et al., 2020; Cunningham & Lekic, 2020; Kim et al., 2023).

We construct a new sediment layer model for the SLB by jointly inverting the RF and Rayleigh-wave measurements at each station (Figure 1). This joint inversion constrains both the velocity at shallow depths and the depth of prominent seismic discontinuities such as R2. The latter was not resolved in the previous surface wave analysis (Zeng et al., 2022).

2. Data and Methods

2.1. Seismic Networks in the Salt Lake Basin

We use all available stations in the SLB for the time period 2000 to 2023 for analyzing the basin velocity structure (Figure 1). These stations are from the University of Utah Regional Seismic Network (University of Utah, 1962), the United States National Strong Motion Network (U.S. Geological Survey, 1931), and three temporary geophone arrays that were deployed in 2018, 2020, and 2023. The array in 2018 consisted mostly of stations that were installed along a 2.9 km east–west line that crosses the EBF (Lin & Kim, 2018). In 2020, a nodal array was operated for one month to monitor the aftershock sequence of the 2020 Magna earthquake (Allam, 2020; Pankow et al., 2020). In 2023–2024, nodal stations were deployed for a few months to a year to collect data on spatio-temporal groundwater variations in the SLB (Zeng & Lin, 2023).

2.2. Receiver Function Analysis

We utilize teleseismic P-waves from earthquakes in the USGS PDE catalog of magnitude ≥ 6.5 at epicentral distances between 25° and 90° that occurred between January 2000 and May 2023. Only teleseismic waveforms with signal-to-noise ratios (SNRs) larger than $\sqrt{5}$ in both radial and vertical components are used for the RF analysis. The SNR is measured by taking root-mean-square ratios between 70-s-long signal and 70-s-long pre-

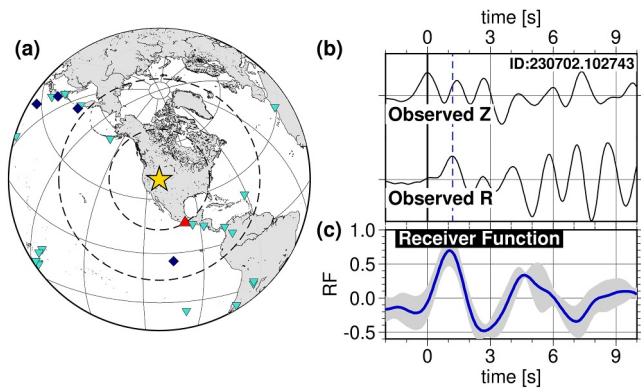


Figure 2. (a) The distribution of teleseismic earthquakes used for the receiver function (RF) analysis with the temporary arrays. The red triangle, dark blue diamonds, and turquoise inverted triangles mark the events used for the three nodal arrays in Figure 1, with matching map symbols. The yellow star is the location of the Salt Lake basin (SLB). The dashed circles indicate 30° and 60° distances from the study region. (b) Vertical- (Z) and radial- (R) component P-wave records of a teleseismic event on 2 July 2023, from station 501 within the 2023 array (Figure 1). The vertical thick black solid line marks the time of the first peak on the Z component. The vertical thin blue dashed line marks the time of the first peak on the R component, which is measured relative to the time of the first Z component peak. (c) The average of the RFs at the same station, shown as a blue solid curve with the gray shade marking $\pm 2\sigma$, where σ is the standard deviation of the RF stack estimated by bootstrap resampling.

signal time windows in the 0.1–1.0 Hz frequency band after removing the instrument response. Owing to the short operation times of the geophone arrays, only a few teleseismic events are available for the analyses with these arrays (Figure 2a). The number of teleseismic events used by a permanent network station varies from ~ 20 to ~ 120 . We deconvolve the vertical component from the radial component of the teleseismic P-wave record using the extended-time multi-taper correlation method (Shibutani et al., 2008). In applying this deconvolution method, we use time windows relative to the theoretical P-wave arrival time of -35 to $+102.5$ s for the signal and -135 to -35 s for the pre-signal noise. The RFs are Gaussian low-pass filtered ($e^{-\omega^2/4a^2}$) with $a = 3.5$, which corresponds to a corner frequency of 0.81 Hz. We discard RFs with RF SNR lower than 1.2 to avoid RFs affected by deconvolution instability.

The RFs in the SLB show evidence of a strong, shallow impedance contrast that we interpret as R2, the discontinuity at the base of the semi-consolidated sediments. The Ps phase from this discontinuity is likely the first significant peak in the radial component, which is delayed from the first peak in the vertical component (Figure 2b). The time difference between the first significant peaks in the vertical (i.e., direct P) and the radial components (Ps) (Figure 2b) is approximately equivalent to the time delay observed in the RF (Figure 2c). This peak delay is a robust feature in stations with multiple RFs as illustrated by the small standard deviation of the RF stack in Figure 2c. To determine the RF peak delay time, we measure the time of the largest amplitude peak within the time window -0.1 to 2.5 s.

2.3. Rayleigh Wave Measurements

We combine the RF observations with the Rayleigh wave measurements made by Zeng et al. (2022) using the 31 March 2020 M_w 6.5 Stanley, Idaho, earthquake. The measurements include station-specific 5- to 20-s period H/V measurements, valley-average phase velocities, and their associated uncertainties. The Zeng et al. (2022) H/V measurements and the RF peak delay times observed in this study show a positive correlation (Figure 3). This correlation suggests that both measurements are sensitive to the same structural feature—the shallow basin sediments—making them suitable for joint inversion. We note that the Rayleigh wave H/V measurements are only available for stations in the 2020 array and the UU network. For other station sites, we estimate H/V by taking the Gaussian-weighted average of nearby station measurements, using a standard deviation of 2 km and considering only measurements within a 6 km radius. The interpolated value is used only when more than two samples are available within this distance.

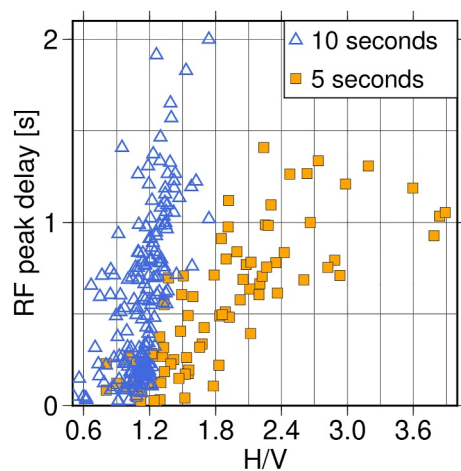


Figure 3. Plot of RF peak delay time versus H/V. Data points for H/V measurements at 5-s and 10-s period are shown as orange squares and open blue triangles, respectively.

2.4. Data Compared to WFCVM Predictions

We compare the observed RF peak delay time and H/V values with the predicted values from the WFCVM at each station (Figure 4). At each station, we extract the 1D model from the WFCVM and use it to calculate the RF and period-dependent H/V values (Takeuchi & Saito, 1972; Thomson, 1950). There are some differences between the measured and predicted RF peak delay times (Figures 4a and 4b) and where they occur, the measured values are generally higher. Most notably, in the area between the EBF and the WVFZ the observed values are roughly twice as high as the predicted ones. For the Rayleigh wave H/V, the observed values at 10-s period (Figure 4c) have a larger range than the predicted values (Figure 4d). More specifically, the observed values are smaller in the mountains and higher in between the EBF and WVFZ. These discrepancies highlight areas where the WFCVM is not an accurate representation of the actual velocity structure.

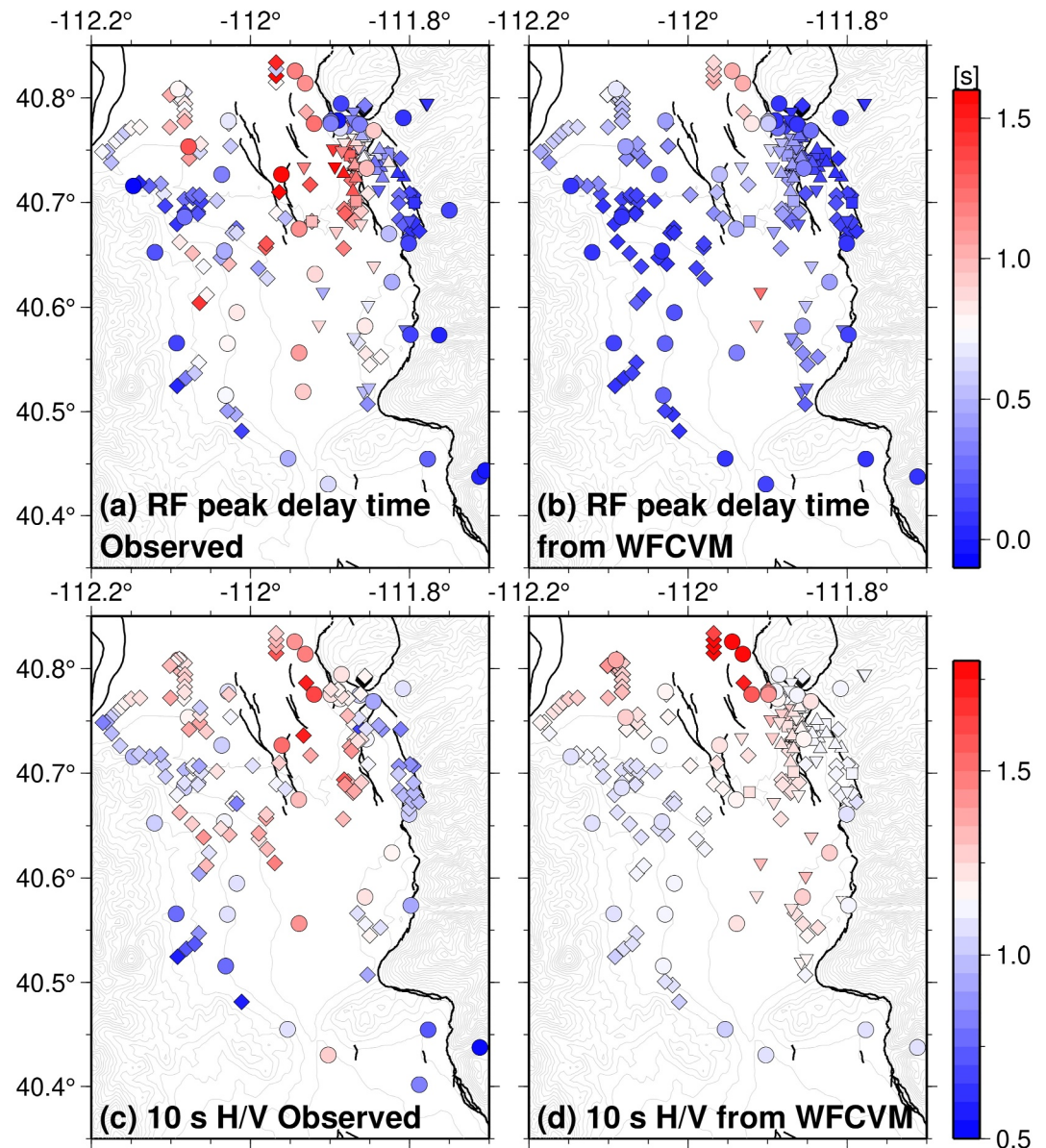


Figure 4. Maps showing comparisons between observations and predictions computed from station-specific 1D velocity models extracted from the Wasatch Front community velocity model (WFCVM). (a) Observed and (b) predicted RF peak delay times. (c), (d) Same as (a), (b) but for 10-s Rayleigh wave H/V. The station symbols are the same as in Figure 1.

3. 1D Bayesian Receiver Function and Surface Wave Joint Inversion

3.1. Bayesian Inversion Method

We employ the Bayesian inference technique (Bayes, 1763) to search for 1D shallow crustal models (\mathbf{m}) that explain both the Rayleigh wave measurements and the RFs. We solve the nonlinear inverse problem $\mathbf{d} = \mathbf{g}(\mathbf{m})$ through repeating forward calculations, where \mathbf{d} is the data vector including Rayleigh wave phase velocities, H/V measurements, and a 20 sample per second RF waveform. $\mathbf{g}(\mathbf{m})$ is the synthetic data vector computed using the model vector, \mathbf{m} , containing structural model parameters such as layer thicknesses and velocities. The solution to this inverse problem is given by a posterior probability density (PPD) function of the model parameters (e.g., Figures 5 and 6).

The model PPD function is obtained using the Markov chain Monte Carlo (MCMC) approach with the Metropolis–Hastings Algorithm (Bailer-Jones, 2017). Bayes' theorem defines the posterior probability $P(\mathbf{m}|\mathbf{d})$, which is the probability of the model \mathbf{m} given the data \mathbf{d} , as follows:

$$P(\mathbf{m}|\mathbf{d}) \propto P(\mathbf{d}|\mathbf{m})P(\mathbf{m}), \quad (1)$$

where $P(\mathbf{m})$ is the prior probability of model \mathbf{m} and $P(\mathbf{d}|\mathbf{m})$ is the probability of the data given model \mathbf{m} (i.e., the model likelihood). The likelihood of each input is given by

$$P(\mathbf{d}_{\text{input}}|\mathbf{m}) = \prod_{k=1}^{N_{\text{data}}} \frac{1}{\sqrt{2\pi}\sigma_k} \exp\left(-\frac{(d_k - s_k)^2}{2\sigma_k^2}\right), \quad (2)$$

where N_{data} is the number of data points d_k , s_k is the synthetic data, and σ_k is the standard deviation of the data noise. For surface waves, d_k and s_k are the observed and synthetic Rayleigh wave H/V and phase velocity values and σ_k are their associated uncertainties. The synthetic Rayleigh wave H/V and phase velocities are calculated following Takeuchi and Saito (1972).

For the RFs, d_k is the observed RF time series, s_k is the synthetic RF time series computed from model \mathbf{m} , and σ_k is the standard deviation of the observed RF stack estimated via the bootstrap resampling method. If only a single RF is available, so that we cannot calculate the standard deviation of the RF stack, we use the pre-signal root-mean-square of the RF for σ_k . In this study, we use the RF waveform in the first peak time window, which we define as the time interval between the first zero crossings before and after the maximum amplitude RF peak between -0.1 and 2.5 s. For synthetic data, the vertical and radial synthetic waveforms are calculated using the propagator matrix method following Thomson (1950), and the RF is calculated by the same deconvolution method applied to the data. The data input and synthetic RF time series are normalized by their maximum amplitude to eliminate absolute amplitude information.

The joint inversion method employed in this study takes advantage of the complementary sensitivities of the Rayleigh wave data and the RFs. The time of the first peak of the RF is sensitive to the S-wave travel time within the sediment layers above the R2 discontinuity. The set of Rayleigh wave H/V values at 5- to 20-s periods is sensitive to the S-wave velocities of both the sediments and the bedrock and the contrast between them at R2. The Rayleigh-wave phase velocity constrains the deeper bedrock velocities. Combining these three data sets reduces the trade-off between the thicknesses and velocities of the sedimentary layers in our velocity model.

3.2. Inversion Steps

The joint inversion is performed in three steps. The first step is using the valley-average phase velocity measurements from Zeng et al. (2022) to invert for the reference 1D velocity structure to set the prior probability of the model. We test various assumed numbers of constant velocity layers ($N = 2$ to 5) to decide on the minimum number of layers appropriate for the inversion without overfitting the data. The results of our initial inversions for layer velocities and thicknesses show significant trade-offs between parameters. However, the overall median

probability density profiles (Figure S1 in Supporting Information S1) for three or more layers do not show any significant changes in the depth to the top of the bottom layer (~ 8 km) and the V_S of the bottom layer. The three layer ($N = 3$) inversion has a mode value of V_S in the second layer of ~ 3 km/s, which is within the velocity range of bedrock. Consequently, we assume four layers ($N = 4$) for the station-specific joint inversions to allow the top two layers to model the unconsolidated and semi-consolidated sedimentary layers. The V_S of the third and fourth (bottom) layers are fixed to the mode value of V_S from the four-layer phase velocity inversion and the depth to the top of the bottom layer is fixed (Table 1). The P-wave velocity and density are derived from V_S using the relationship in Brocher (2005). The phase velocity is not used further for the station-specific inversions.

In the remaining two steps, we invert for the V_S and thicknesses of the top two layers at each station either using the H/V measurements only (step 2) or

Table 1
Search Ranges of Inversion Parameters

Layer no.	Thickness (H) [m]	S-wave velocity [m/s]
1	50–4,000	234–2,282
2	100–4,000	337–3,382
3	8,000 – H_1 – H_2	3,382
4	half-space	3,962

Note. Search ranges of inversion parameters for the step 2 and step 3 inversions. The thickness of the third layer depends on thicknesses of the first and second layers. The velocities of the third and fourth layers are fixed. The P-wave velocity (V_P) and density (ρ) are determined using relationships in Brocher (2005).

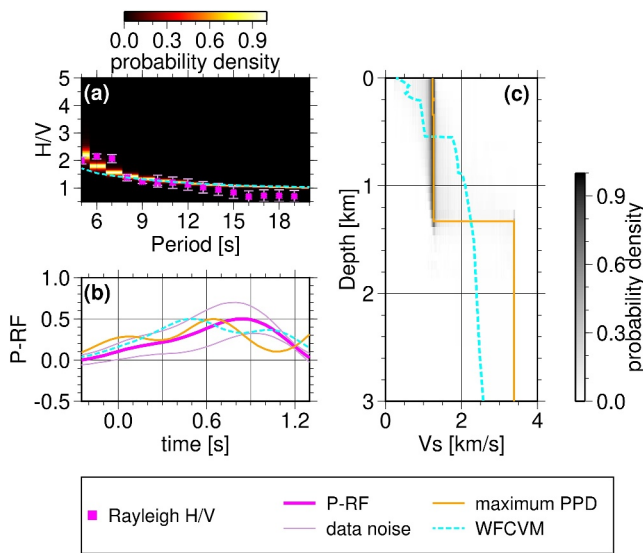


Figure 5. Result of the step 2 inversion at station SSC (Figure 1) using the H/V measurements. (a) The observed (“Rayleigh H/V”) and predicted H/V. The magenta squares with light purple error bars show the input data with $\pm 1\sigma$ uncertainties. The background color represents the posterior probability density (“PPD”) distribution of the synthetic H/V for the set of trial models in (c), with lighter colors indicating higher probability and vice versa. The cyan dashed line indicates predicted H/V values using the WFCVM. (b) The observed (“P-RF”) and predicted RF waveforms. Similar to (a), the thick magenta line, light purple enclosed region, and cyan dashed line represent the observed RF, its corresponding uncertainty, and the predicted RF from the WFCVM, respectively. The orange solid line is the predicted RF using the final inverted model shown in (c). (c) The PPD distribution of the shear-wave velocity (V_s) as a function of depth from the inversion, with the maximum probability Versus profile shown as a solid orange line. The cyan dashed line is the shear-wave velocity profile from the WFCVM.

using both the H/V and the RF (step 3). For step 2, we select an arbitrary initial model with 1,250 and 2,750 m/s Versu in the top two layers and a 500-m thickness for each. Because we extensively search across the model space, the selection of the initial model does not affect the final posterior model distribution. For step 3, the initial model is based on the mode (maximum probability) model parameters derived from step 2. While using an initial model with relatively good data fit doesn't affect the final posterior model distribution, it avoids random walks in model space with poor data misfit and hence reduces computation cost. To prevent overfitting the 20-sample-per-second RF waveform, we upscale the RF uncertainty by the square root of the ratio between the number of data points in the RF and those in the H/V data set.

We employ Parallel Tempering (Sambridge, 2014) in the inversion to conduct an efficient global search throughout the model space. The likelihood of multiple MCMC iteration chains running in parallel is calculated with an exponent of the inverse of temperatures (i.e., $P(m)^{1/T}$). We use 40 chains running in parallel, with 25% of the chains having unity temperature ($T = 1$). The other chains have random temperatures between $T_{\min} = 1$ and $T_{\max} = 4,500$. The number of iterations is 1.6×10^5 with the burn-in period set as 1.3×10^5 iterations, which is about 70% of the total number of iterations. A larger number of iterations is used if the convergence is not reached within 1.6×10^5 , which occurred for only a few stations.

3.3. Sediment Layer Models From the Joint Inversion

Figures 5 and 6 show examples of the step 2 and three inversions using measurements from station SSC (UU network). The high H/V values at and below 7 s period are not well predicted by the WFCVM (Figure 5a). The inverted Versus model from step 2 shows a velocity jump at a 1.2-km depth, which is considerably deeper than the 0.5-km depth of the largest velocity jump in the WFCVM at R2 (Figure 5c). However, neither the WFCVM nor the inverted Versus model from step 2 predict the initial peak RF waveform very well (Figure 5b).

The inverted model from step 3, while keeping the H/V misfit similar to that of step 2, reduces the RF misfit considerably (Figure 6). The model reveals two seismic discontinuities at approximately 0.2- and 1.2-km depths. The shallower discontinuity is roughly at the same depth as the R1 discontinuity in the WFCVM. The deeper discontinuity, consistent with the result in step 2, is more than twice as deep as the R2 discontinuity in the WFCVM. The timing of the first RF peak roughly corresponds to the expected Ps phase excited at the 1.2-km depth discontinuity. The Ps phase generated at the 0.2-km depth discontinuity is included within the width of the first RF peak and contributes to fitting the observed RF. The inversion examples in Figures 5 and 6 demonstrate the complementary sensitivity of the RF and H/V data to the shallow basin structure and show how the joint inversion of the two reduces the non-uniqueness of the inverted model.

We evaluate the data misfit for each inversion based on the likelihoods calculated from Equation 2 (Figure 7). In this study, we construct the inverted model following each step based on the maximum posterior probability for each model parameter. We note that due to tradeoffs among different parameters, the inverted model defined in this way may be quite different from the model that produces the minimum misfit (or maximum likelihood), particularly when a multimodal posterior model distribution is present. As expected, the H/V likelihoods are generally higher than the RF likelihood for models inverted in step 2 (Figures 7a and 7b) as only H/V is used in the inversion. Some stations have low H/V likelihoods in Figure 7a, which probably reflects strong trade-offs and non-uniqueness of the inverted models. Clear improvement of both H/V and RF likelihoods is observed for the models obtained in step 3 (Figures 7c and 7d). This improvement shows that the inverted models from step 3 can explain both H/V and RF data simultaneously and suggests that the joint inversion of the two data sets suppresses tradeoff and model non-uniqueness.

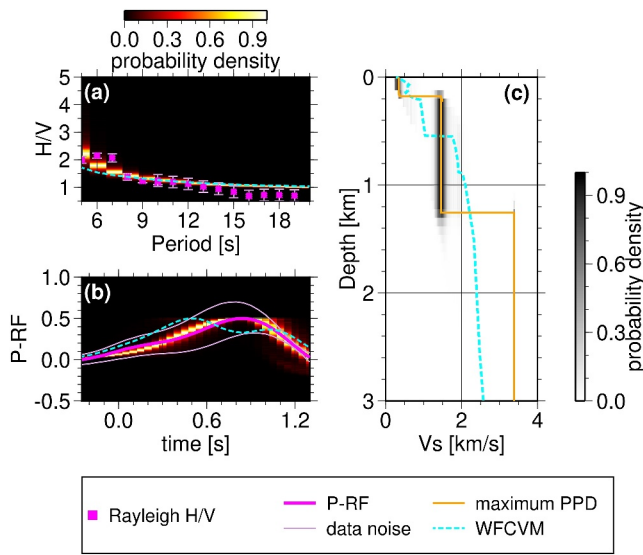


Figure 6. Same as Figure 5 but for the step 3 inversion. (a) The observed (“Rayleigh H/V”) and predicted H/V ratios. (b) The observed (“P-RF”) and predicted RF waveforms. The background color represents the posterior probability density (“PPD”) distribution of the synthetic RF for the inverted posterior model distribution shown in (c), with lighter colors indicating higher probability and vice versa. (c) The PPD distribution of the inverted Versus model. The presentation follows the description in Figure 5 caption, except for the background colors in (b).

4. Results

4.1. Depth to the R2 Discontinuity Across the SLB

We computed RFs and incorporated them into our inversion in order to address the absence of the R2 discontinuity when inverting surface wave measurements alone (Zeng et al., 2022). Here, we define the depth of the R2 discontinuity as the depth at which the shear-wave velocity reaches 1.5 km/s, consistent with Versus values below the R2 boundary in the WFCVM. The depths to R2 in our model, in the WFCVM, and in Zeng et al. (2022), all determined using the Versus = 1.5 km/s definition, are illustrated in Figures 8a–8c. Note that in Zeng et al. (2022), Gaussian smoothing was applied to interpolate measurements onto grid points. Here, we refrain from interpolating our 1D models to preserve the maximum lateral resolution achievable with our data. Therefore, instead of presenting an R2 map, we only show R2 depths at specific station locations for our seismic inversion model (Figure 8c). In the next section, we discuss how R2 depth coverage can be further improved through joint analysis of seismic and gravity observations (Figure 8d).

The presence of a deep basin in the northeastern part of the valley (north of 40.75°, from −112° to −111.9°) and thin sediments along the western and eastern margins of the valley are consistent features of all models shown in Figure 8. Clear differences, on the other hand, are observed in the area bounded by the WVFZ and the EBF where R2 depths are significantly shallower in the WFCVM compared to other models. Moreover, the R2 depths in the southernmost part of the valley (south of 40.58°) are also shallower in the WFCVM. The well logs and seismic active source profiles

used to construct the WFCVM were primarily located in areas with thin sediments, which might explain the overall bias toward thinner sediments for the WFCVM. It is perhaps not surprising that the R2 depths of Zeng et al. (2022) and our new model share many common features as they share the same surface wave data set. Benefiting from the exceptional lateral resolution of RFs and their sensitivity to velocity discontinuities, our new seismic model (Figure 8c) shows more pronounced lateral and vertical velocity variations, such as the sharp changes across the EBF and WVFZ.

4.2. Joint Interpretation With Gravity

Like our seismic measurements, the CBGA for the SLV area (Figure 9a; Pan-American Center for Earth and Environmental Studies, 2012) is sensitive to R2 depth, owing to the density contrast between the unconsolidated and semi-consolidated sediments and the underlying bedrock. The most common way to convey and interpret gravity data is with the CBGA. The CBGA quantifies the difference between the observed gravity and the gravity predicted from a crustal model of constant density. The anomaly calculation applies the following corrections: theoretical gravity, free air, Bouguer slab, and terrain effects. The CBGA in this study was computed using a reduction density of 2.67 g/cm³ and the formulas outlined in Hinze et al. (2005). However, applying a regional gravity correction is crucial to account for long-wavelength gravity variations that arise from deeper, large-scale structures rather than the local basin sediments. To accomplish this task, we tested different regional gravity representations by fitting the CBGA with polynomials of degrees ranging from 0 to 16. We determined that the degree-3 polynomial (Figure 9b) produces the best correlation between the residual gravity (CBGA minus regional), hereafter referred to as SLB local gravity (Figure 9c), and our RF peak delay times (Figure 4a) with a correlation coefficient near −0.6 (Figure S2 in Supporting Information S1). Based on this analysis, we selected the degree-3 polynomial fit to the CBGA as our regional gravity correction. Note that this correction was determined from the gravity data alone. We used the seismic data only to guide the choice of the degree of the polynomial fit to the gravity data. It is appropriate to use the seismic data for this purpose since the variations of both the RF peak delay times and the local gravity field are due primarily to variations in sediment thickness. We note that our regional gravity correction is significantly different from the one applied by Radkins (1990) before he inverted his gravity data for the R2 depths used in the WFCVM.

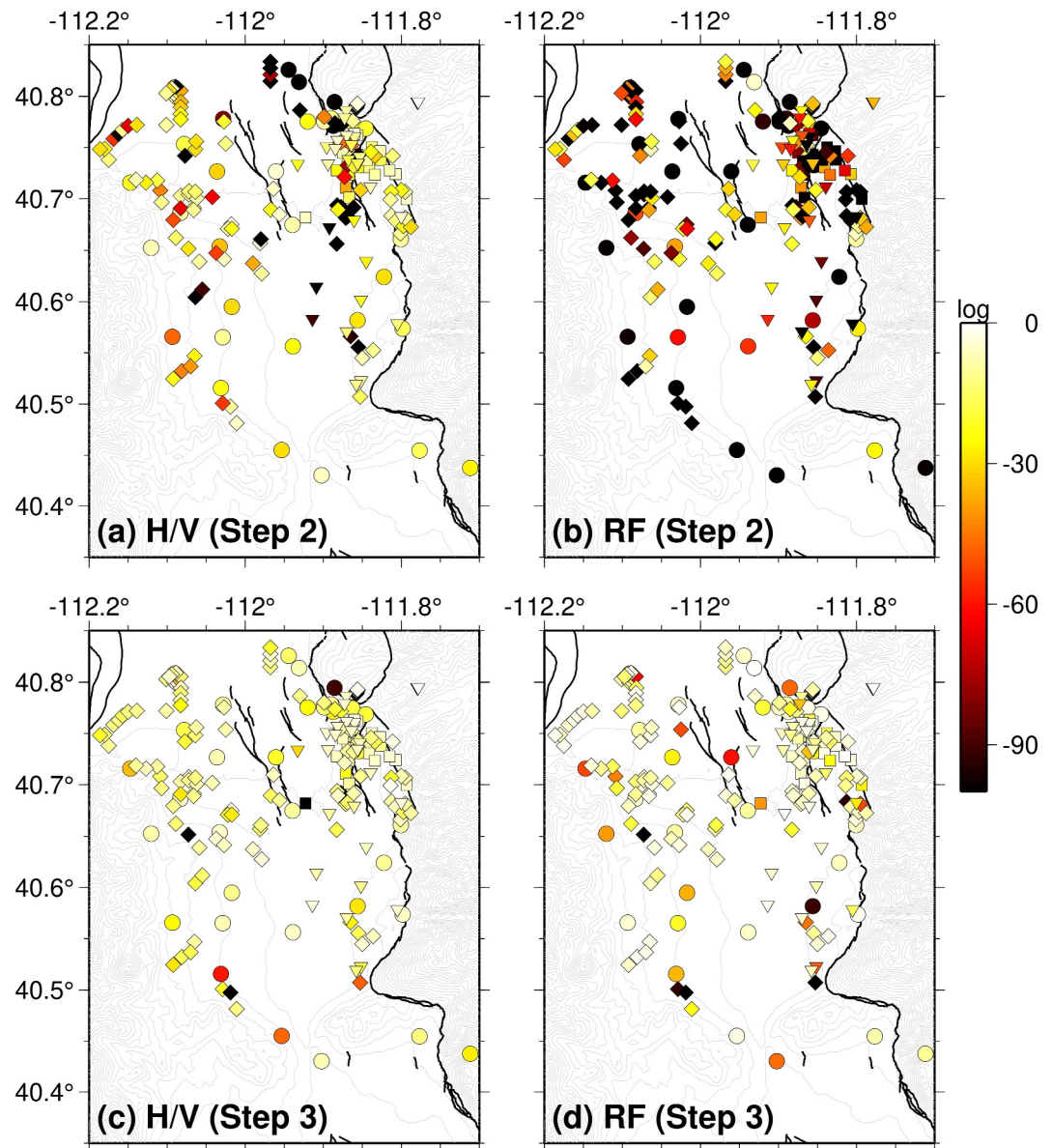


Figure 7. Maps of log-likelihoods of the inverted models. (a) The H/V log-likelihoods for models inverted in step 2. Lighter colors indicate higher log-likelihoods, and vice versa. (b) The same as (a), but for the RF log-likelihoods. (c)–(d) The same as (a)–(b), but for models inverted in step 3. The symbols match the map symbols in Figure 1.

We predict gravity anomalies across the SLB using the density parameters in both our inverted model and the WFCVM. For each station location, we assume the 1D structure extends laterally to form computationally infinite slabs. We remove the mean gravity value from all station locations to obtain the gravitational anomalies. The gravity anomalies predicted by our new model (Figure 9e) show a stronger correlation with the SLB local gravity (Figure 9c) than the gravity anomalies predicted from the WFCVM (Figure 9d). The new velocity model provides reasonably good predictions of the gravity lows between the WVFZ and the EBF between 40.65 and 40.80°, the gravity low in the southern part of the valley (south of 40.65°), and the gravity variations along the western margin of the valley. The WFCVM, on the other hand, clearly underpredicts the amplitude of the observed gravity variations throughout the valley (Figures 9d and 10). Discrepancies between predictions and observations in both seismic (Figure 4) and gravity data (Figure 9) highlight areas of the WFCVM that need revision.

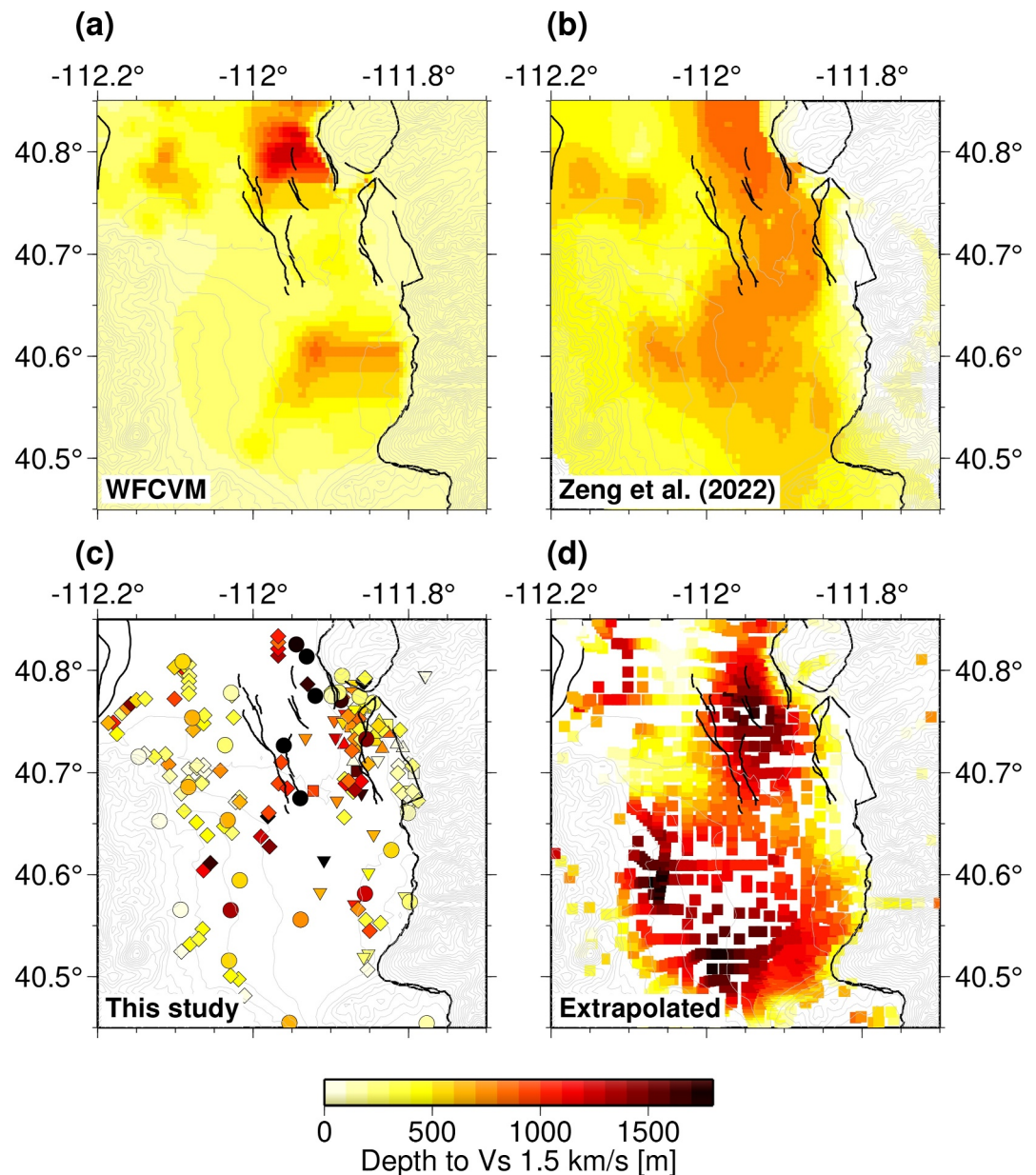


Figure 8. R2 depths (depth to $v_s = 1.5$ km/s) across the SLB. (a) The R2 depths from the WFCVM (Magistrale et al., 2008) (b) The R2 depths from Zeng et al. (2022). (c) The R2 depths determined by the station-specific 1D velocity inversions performed in this study. (d) The R2 depths calculated from the linear relationship between the R2 depths in (c) and the SLB local gravity in Figure 9c (Figure 9f).

Despite the positive correlation, a detailed examination suggests that our new model slightly overpredicts the amplitude of the observed gravity variation (Figure 10). This observation suggests that the actual density contrast between the sediments and the bedrock is smaller than the density contrast in our model. As our seismic inversion is mostly sensitive to the S-wave velocity, the density model is only retrieved through the velocity-density empirical relation in Brocher (2005) (Figure S3 in Supporting Information S1). We suspect that this empirical relation is less accurate in the SLB due to the high groundwater content of SLB sediments, which reduces Versus significantly but has less impact on density.

Given the strong correlation between the gravity field and our inverted seismic model, we use the more extensive gravity data coverage to estimate R2 depths in areas lacking seismic stations. We obtain SLB local gravity at all of

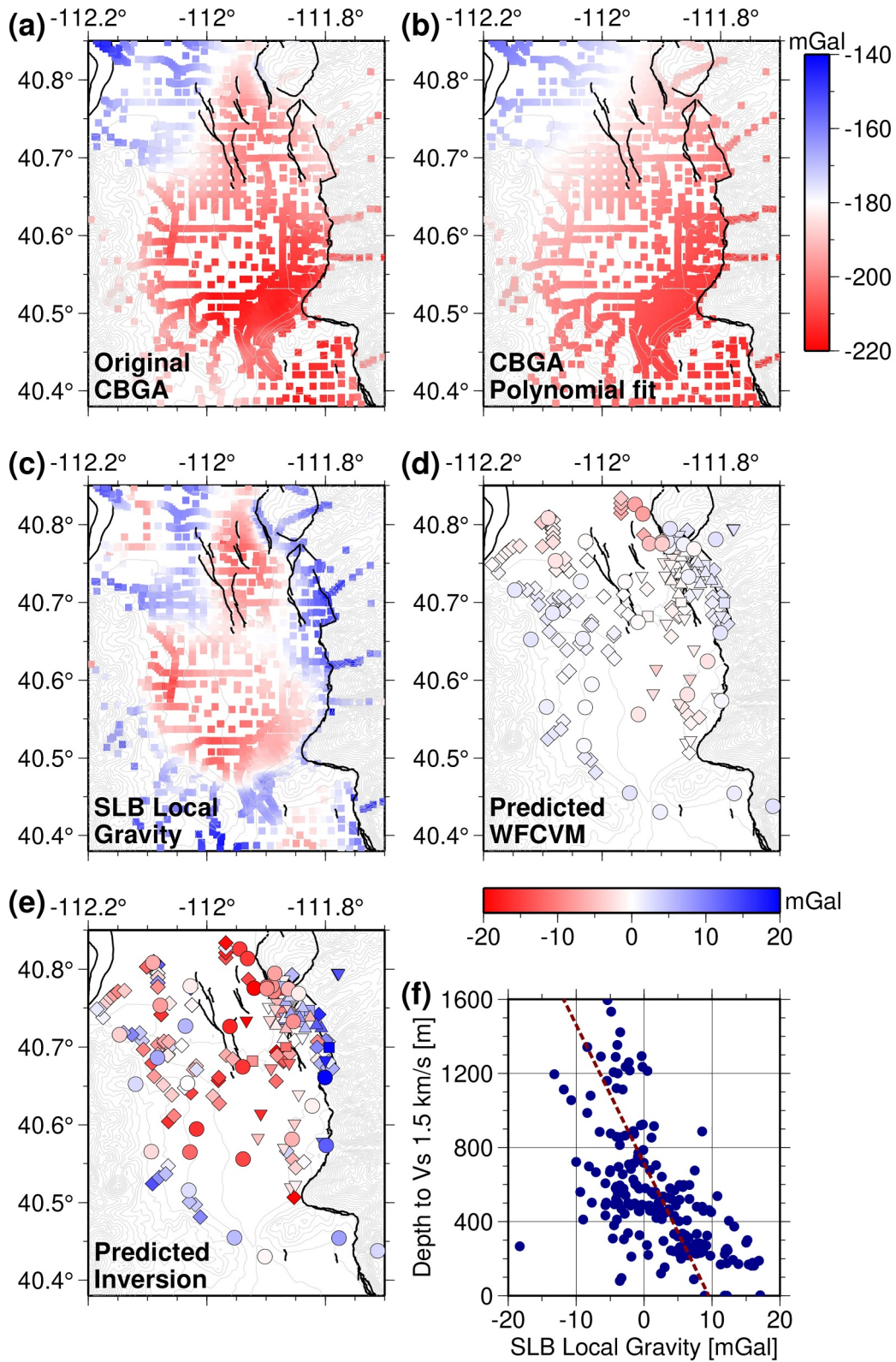


Figure 9.

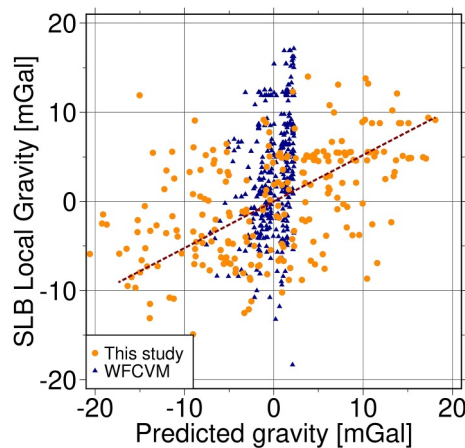


Figure 10. Plot of demeaned SLB local gravity versus demeaned gravity predictions determined with the velocity model from this study (orange circles) and the WFCVM (blue triangles). The linear fit (dotted red line) was obtained by orthogonal regression of the orange circles and has a slope of 0.52.

the seismic stations by interpolating the SLB local gravity in Figure 9c. We then establish a linear relation between our inverted R2 depths and the SLB local gravity (Figure 9f) by orthogonal regression (Cheng & Van Ness, 1999, pp. 9–11; Castellaro et al., 2006; Castellaro & Bormann, 2007). We apply this linear relation to estimate R2 depths below every site in the SLB where a gravity reading is available (Figure 8d). We note that the R2 depth map constructed this way is smoother and shows less lateral variation than the R2 depth map from our station-specific seismic inversion (Figure 8c) in places where the seismic station coverage is good. This smoothing occurs because of the intrinsic non-linear character of the gravity field, for which resolution and sensitivity fall off with distance/depth (d) as $\sim d^{-2}$.

5. Discussion

5.1. Implications of the New Sediment Thickness Model

Thicker sediments generally lead to larger ground motion amplitudes, especially at longer periods, as demonstrated by studies in southern California (Day et al., 2008; Denolle et al., 2014) and in the SLB (Moschetti et al., 2021; Wang et al., 2017). Therefore, the deeper R2 depths observed in the new model suggest the potential for larger ground shaking compared to predictions

made using the WFCVM. Notably, the increase in R2 depths is concentrated between the WVFZ and the EBF, a heavily populated area, which adds to the importance of considering our new model in future shaking predictions.

Hutchings (2023) reported that in the frequency range 0–3 Hz, numerical simulations of an M_w 5.7 earthquake with the WFCVM underpredicted peak ground motions in the northeastern part of the SLB, between the WVFZ on the west and the East Bench and Warm Springs faults on the east. This area is the same general area where our model shows deeper R2 depths than the WFCVM. Hutchings's (2023) results provide some support for the larger R2 depths in our model relative to the WFCVM. However, additional work would be needed to show that numerical simulations with our model provide a better fit to earthquake records than simulations with the WFCVM.

Our R2 depths indicate that the R2 depths in the WFCVM are inaccurate in some parts of the SLB and should be corrected. These inaccuracies are probably due, in part, to the limited number and uneven distribution of R2 depth constraints that Radkins (1990) used for his gravity inversion, which provided the R2 depths for the SLB part of the WFCVM (Figure S4 in Supporting Information S1). Radkins's R2 depth constraints came from seismic reflection profiles and wells located mostly around the edges of the basin, where we expect relatively shallow R2 depths. Another potential source of error in the WFCVM is the lithologic well logs which supplied the R2 depth constraints over most of the SLB. Some of these lithologic logs were recorded by water well drillers, not geologists. These driller's logs “may be somewhat less usable for geologic purposes” according to Case (1985), the primary source for the well logs used by Radkins (1990).

In Figures S5 and S6 in Supporting Information S1, we show our inversion results for two stations along with R2 depths determined from lithologic logs for water wells within a 1 km radius of these stations. As illustrated in Figure S5 in Supporting Information S1, our 1D seismic inversion results for station 130 near the eastern edge of the basin (Figure S4 in Supporting Information S1) give an R2 depth of 0.287 km. This depth is in reasonably good agreement with the R2 (“bedrock”) depth of 0.121 km taken from the driller's log for a nearby well. The small difference of 0.166 km could be due to lateral heterogeneity, inaccuracies in the Brocher (2005) V_p/V_s relation assumed in this study, and/or a misidentification of “bedrock” in the well log. Figure S6 in Supporting Information S1 shows our inversion results for station 031, which is located near the middle of the SLB (Figure S4 in Supporting Information S1). The R2 depth of 0.902 km from this inversion is much larger than the R2 depth of

Figure 9. Observed and predicted gravitational anomalies across the SLB. (a) The complete Bouguer gravity anomaly (CBGA) (Pan-American Center for Earth and Environmental Studies, 2012). (b) The degree three polynomial fit to the CBGA. (c) The SLB local gravity, which is the difference between the CBGA in (a) and the regional correction in (b). (d) The demeaned predicted gravity anomaly obtained using the WFCVM at locations with seismic stations. (e) Same as (d) but using the model from this study. (f) Plot of R2 depth in Figure 8c versus the SLB local gravity in (c). The dark red dashed line is the best fitting line determined by orthogonal regression, $y = -74.8x + 714$. All color bar units are mGal.

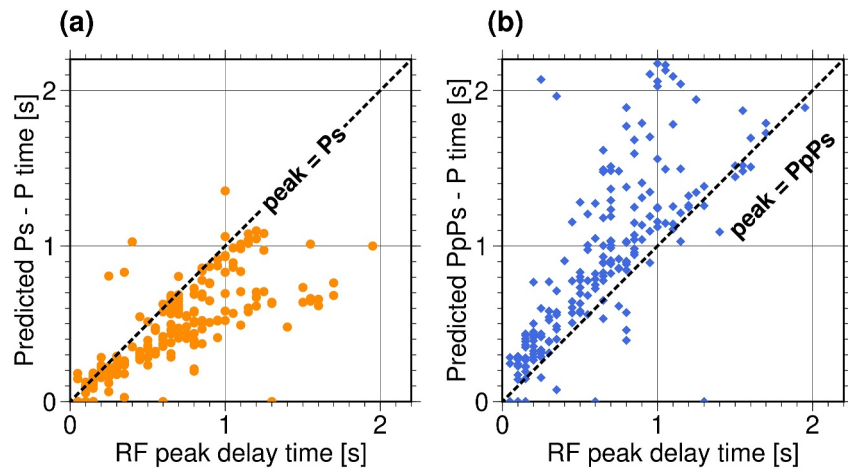


Figure 11. Plots of predicted Ps-P (a) and PpPs-P (b) times versus synthetic RF first peak delay times. The predicted times are all calculated for the set of 1D models determined in this study. The phase conversions and reflections are assumed to occur on the R2 interface. The black dashed line is the line of agreement.

0.130 km interpreted from a driller's lithologic log for a nearby water well. However, this lithologic log has some inconsistencies (described in the caption for Figure S6 in Supporting Information S1) which suggest that the R2 depth that Radkins (1990) obtained from it might not be correct.

5.2. Complications of Using RFs to Determine Sediment Thicknesses

This study also has implications for using RFs for imaging sedimentary basins. In principle, if the target area has a homogeneous, thick, and slow sediment layer the RF peak delay time will correspond to the P-to-s converted phase Ps. However, for a thin and complicated (e.g., multi-layered) sediment structure, the direct P-wave, the Ps phase, and later multiple phases such as PpPs (described below) may not be well separated in the time domain RFs. Moreover, the relative dominance of their amplitudes depends on the structure, making it difficult to judge which phase corresponds to the maximum peak in the time window. Hence, a correspondence of peak delay time to the Ps phase is not always assured.

To better demonstrate this problem, in Figure 11 we plot the predicted R2 Ps-P and PpPs-P times versus the peak delay time of the synthetic RFs. All of these times are computed for the final set of 1D models of this study. The PpPs phase is a multiple that crosses a seismic discontinuity as a P wave, reflects off the surface as a P wave, and then converts to an upgoing S wave at the discontinuity before traveling back up to the surface (Zhu & Kanamori, 2000). On the plot comparing the Ps-P time with the peak delay time (Figure 11a), two branches are clearly observed. Only the points in one branch lie close to the line of perfect agreement. The other branch has Ps-P times smaller than the peak delay times, suggesting that the first RF peak does not correspond to the Ps phase. For these points, the PpPs-P time is more similar to the peak delay time (Figure 11b). This observation implies that at some stations, the first large RF peak is the PpPs phase rather than the Ps phase. This analysis demonstrates the potential ambiguity of identifying the correct phase for the first RF peak and shows the value of the RF waveform fitting approach adopted in this study.

6. Summary and Conclusions

We conducted a joint inversion of RF waveforms, Rayleigh wave H/V ratios, and Rayleigh wave phase velocities to construct a set of 1D velocity models for the top 8 km of the SLB. Compared to the WFCVM, we show that our 1D model set better explains not only the seismic data but also the SLB local gravity data. Moreover, our model reveals a deeper R2 (semi-consolidated sediment to bedrock interface) in several areas, particularly in the heavily populated part of the Salt Lake City metropolitan area located between the EBF and the WVFZ. The presence of thicker sediments suggests a potential for greater ground shaking during strong local earthquakes. Our findings may be consistent with the underestimation of peak ground motions in the northeastern SLB from the 2020 Mw

5.7 Magna earthquake by numerical simulations using the WFCVM. The seismic observations and models presented in this paper identify opportunities to improve the WFCVM in the earthquake-prone SLV area.

RF analysis, while subject to limitations such as trade-off and non-uniqueness, has proven to be an effective tool to find and map sedimentary interfaces with significant impedance contrasts. The RF method's non-intrusive nature makes it particularly attractive for applications in urban areas such as Salt Lake City. Although only a few good teleseismic events are usually recorded during a typical month-long nodal geophone experiment, we show that RF first peak waveforms derived from these teleseisms are quite stable and reliable for shallow imaging studies. Furthermore, because the piercing point of RFs is almost directly beneath the station location for shallow velocity discontinuities, RF has the advantage of mapping such discontinuities with high horizontal spatial resolution. Combining RFs with other measurements that are also sensitive to shallow sedimentary structure, such as Rayleigh wave H/V ratios and gravity, helps to suppress the trade-off between different model parameters which causes non-uniqueness of the models.

Data Availability Statement

The 2018 Linear array data can be found at https://doi.org/10.7914/SN/9H_2018 (Lin & Kim, 2018). The temporary array data sets are available at https://doi.org/10.7914/SN/2A_2020 (Allam, 2020) and <https://doi.org/10.7914/sxpj-9z48> (Zeng & Lin, 2023). The seismic network data from the University of Utah Seismograph Stations (<https://doi.org/10.7914/SN/UU>) and the USGS National Strong motion network (<https://doi.org/10.7914/SN/NP>) can be obtained from the EarthScope Consortium's Seismological Facility for the Advancement of Geoscience Data Management Center (SAGE DMC; <https://ds.iris.edu/ds/nodes/dmc>). The Wasatch Front Community Velocity Model that we used is v3d from the Utah Geological Survey web site (<https://geology.utah.gov/hazards/assistance/consultants/cvm-geophysical/>). The gravity measurements can be obtained from Pan-American Center for Earth and Environmental Studies (2012) and from the Data Collections web site of the Utah Geological Survey (https://geodata.geology.utah.gov/pages/collections_featured.php?parent=650). The inversion code used in this study is available from Github (<https://github.com/seis-hyejeong/rein>) and Kim et al. (2024). Additional details of the inversion method are explained in Kim et al. (2023). The final station specific velocity models are compiled in Kim (2024) in the Zenodo Repository (<https://doi.org/10.5281/zenodo.14010756>).

Acknowledgments

This study was supported by the USGS Earthquake Hazards Program, Award No. G23AP00021. H. J. Kim and F.-C. Lin also acknowledge support from National Science Foundation project EAR 1753362. We thank Emily Kleber of Utah Geological Survey for insightful comments on the gravity and the geology of the study region. We appreciate the work of the student volunteers who helped install the nodes and are thankful to the residents of the SLV area who agreed to host a seismometer for research. Utah Geological Survey staff members Greg McDonald, Stephanie Carney, and Darlene Bataian improved this manuscript through their reviews. We thank Dr. Oliver Boyd, an anonymous reviewer, and the Associate Editor for giving suggestions to improve our manuscript.

References

- Allam, A. (2020). Response to the mar 18, 2020 M5.7 Magna, UT earthquake [Dataset]. *International Federation of Digital Seismograph Networks*. https://doi.org/10.7914/SN/2A_2020
- Baena-Rivera, M., Sánchez-Sesma, F. J., Arciniega-Ceballos, A., Pérez-Rocha, L. E., & Cruz-Jiménez, H. (2023). Ground-Motion similarities in the Valley of Mexico from subduction earthquakes. *Bulletin of the Seismological Society of America*, 113(1), 220–235. <https://doi.org/10.1785/0120220073>
- Bailer-Jones, C. A. L. (2017). *Practical Bayesian inference: A primer for physical scientists*. Cambridge University Press. <https://doi.org/10.1017/9781108123891>
- Bayes, T. (1763). An essay towards solving a problem in the doctrine of chances. *Philosophical Transactions of the Royal Society of London, Series A: Physical Sciences and Engineering*, 53, 370–418. [Reprinted in *Biometrika*, 45, 295–315, 1958].
- Boyd, O. S., Churchwell, D., Moschetti, M. P., Thompson, E. M., Chapman, M. C., Ilhan, O., et al. (2024). Sediment thickness map of United States Atlantic and Gulf Coastal Plain Strata, and their influence on earthquake ground motions. *Earthquake Spectra*, 40(1), 89–112. <https://doi.org/10.1177/87552930231204880>
- Brocher, T. M. (2005). Empirical relations between elastic wavespeeds and density in the earth's crust. *Bulletin of the Seismological Society of America*, 95(6), 2081–2092. <https://doi.org/10.1785/0120050077>
- Bruhn, R. L., Gibler, P. R., Houghton, W., & Parry, W. T. (1992). Structure of the Salt Lake segment, Wasatch normal fault zone: Implications for rupture propagation during normal faulting. In P. L. Gori & W. W. Hays (Eds.), *Assessment of Regional Earthquake Hazards and Risk Along the Wasatch Front, Utah* (pp. H1–H25). U. S. Geological Survey Professional Paper 1500-A-J.
- Case, W. F. (1985). Significant drill holes of the Wasatch front valleys including cache Valley and tooele valley. In *Utah Geological and Mineral Survey Open-File Rep* (Vol. 82). Retrieved from https://ugspub.nr.utah.gov/publications/open_file_reports/OFR-82.pdf, 181
- Castellaro, S., & Bormann, P. (2007). Performance of different regression procedures on the magnitude conversion problem. *Bulletin of the Seismological Society of America*, 97(4), 1167–1175. <https://doi.org/10.1785/0120060102>
- Castellaro, S., Mulargia, F., & Kagan, Y. Y. (2006). Regression problems for magnitudes. *Geophysical Journal International*, 192(3), 913–930. <https://doi.org/10.1111/j.1365-246X.2006.02955.x>
- Cheng, C., & Van Ness, J. W. (1999). *Statistical regression with measurement error*. Oxford University Press, 262
- Chichester, B., Rychert, C., Harmon, N., Allen, R., Collier, J., Henstock, T., & Rietbrock, A. (2020). Seafloor sediment thickness beneath the VoiLA broad-band ocean-bottom seismometer deployment in the Lesser Antilles from P-to-S delay times. *Geophysical Journal International*, 223(3), 1758–1768. <https://doi.org/10.1093/gji/ggaa360>
- Cunningham, E., & Lekic, V. (2020). Constraining Properties of sedimentary strata using receiver functions: An example from the Atlantic coastal plain of the Southeastern United States. *Bulletin of the Seismological Society of America*, 110(2), 519–533. <https://doi.org/10.1785/0120190191>

- Day, S. M., Graves, R., Bielik, J., Dreger, D., Larsen, S., Olsen, K. B., et al. (2008). Model for basin effects on long-period response spectra in southern California. *Earthquake Spectra*, 24(1), 257–277. <https://doi.org/10.1193/1.2857545>
- Denolle, M. A., Miyake, H., Nakagawa, S., Hirata, N., & Beroza, G. C. (2014). Long-period seismic amplification in the Kanto Basin from the ambient seismic field. *Geophysical Research Letters*, 41(7), 2319–2325. <https://doi.org/10.1002/2014GL059425>
- Gkogkas, K., Lin, F.-C., Allam, A. A., & Wang, Y. (2021). Shallow damage zone structure of the Wasatch fault in Salt Lake City from ambient-noise Double beamforming with a temporary linear array. *Seismological Research Letters*, 92(4), 2453–2463. <https://doi.org/10.1785/0220200404>
- Hartzell, S., Carver, D. L., Cranswick, E., & Frankel, A. D. (2000). Variability of site response in Seattle, Washington. *Bulletin of the Seismological Society of America*, 90(5), 1237–1250. <https://doi.org/10.1785/0120000022>
- Hill, J., Benz, H., Murphy, M., & Schuster, G. T. (1990). Propagation and resonance of SH waves in the Salt Lake Valley, Utah. *Bulletin of the Seismological Society of America*, 80, 23–42.
- Hinze, W. J., Aiken, C., Brozena, J., Coakley, B., Dater, D., Flanagan, G., et al. (2005). New standards for reducing gravity data: The north American gravity database. *Geophysics*, 70(2005), J25–J32. <https://doi.org/10.1190/1.1988183>
- Hirakawa, E., & Aagaard, B. (2022). Evaluation and updates for the USGS San Francisco Bay region 3D seismic velocity model in the east and north bay portions. *Bulletin of the Seismological Society of America*, 112(4), 2070–2096. <https://doi.org/10.1785/0120210256>
- Hiscock, A., Kleber, E., McKean, A., Erickson, B., McDonald, G., Giraud, R., et al. (2023). The March 2020, Mw 5.7 Magna, Utah, earthquake—Documentation of geologic effects and summary of new research. *Geology of the Intermountain West*, 10, 113–129. <https://doi.org/10.3171/giw.v10.pp113-129>
- Hutchings, S. J. (2023). Simulation of high frequency ground motion for the 18 March 2020 Mw 5.7 Magna, Utah, earthquake using the Wasatch front community velocity model (WFCVM). In *Master Thesis*. University of Utah. Retrieved from <https://agu.confex.com/agu/fm22/meetingapp.cgi/Paper/1093572>
- Joyner, W. B. (2000). Strong motion from surface waves in deep sedimentary basins. *Bulletin of the Seismological Society of America*, 90(6B), S95–S112. <https://doi.org/10.1785/0120000505>
- Kawase, H. (2003). Site effects on strong ground motions. In W. H. K. Lee, H. Kanamori, P. C. Jennings, & C. Kisslinger (Eds.), *International Handbook of earthquake and Engineering Seismology, Part B*. Academic Press. 1009
- Kim, H. J. (2024). Velocity models from "seismic imaging of the Salt Lake Basin using joint inversion of receiver functions and Rayleigh wave data. Zenodo. <https://doi.org/10.5281/zenodo.14010756>
- Kim, H. J., Kawakatsu, H., Akuhara, T., & Takeuchi, N. (2024). Reverberation waveform inversion software used in "Characterization of Seafloor sediments using teleseismic Body waves recorded by ocean bottom seismometers in the Pacific ocean". Zenodo. <https://doi.org/10.5281/zenodo.10993545>
- Kim, H. J., Kawakatsu, H., Akuhara, T., & Takeuchi, N. (2023). Characterizing the seafloor sediment layer using teleseismic body waves recorded by ocean bottom seismometers. *Journal of Geophysical Research: Solid Earth*, 128(12), e2023JB027616. <https://doi.org/10.1029/2023JB027616>
- Kleber, E., McKean, A. P., Hiscock, A. I., Hylland, M. D., Hardwick, C. L., McDonald, G. N., et al. (2020). Geologic setting, ground effects, and proposed structural model for the 18 March 2020 Mw 5.7 Magna, Utah, earthquake. *Seismological Research Letters*, 92(2A), 710–724. <https://doi.org/10.1785/0220200331>
- Liberty, L. M., St. Clair, J., & McKean, A. P. (2021). A broad, distributed active fault zone lies beneath Salt Lake City, Utah. *The Seismic Record*, 1, 35–45. <https://doi.org/10.1785/0320210009>
- Lin, F.-C., & Kim, H. J. (2018). Salt Lake linear nodal array 2018 [Dataset]. *International Federation of Digital Seismograph Networks*. https://doi.org/10.7914/SN/9H_2018
- Magistrale, H., Day, S., Clayton, R. W., & Graves, R. W. (2000). The SCEC southern California reference three-dimensional seismic velocity model version 2. *Bulletin of the Seismological Society of America*, 90(6B), S65–S76. <https://doi.org/10.1785/0120000510>
- Magistrale, H., Olsen, K. B., & Pechmann, J. C. (2008). Construction and verification of a Wasatch front community velocity model. In *Technical report no. HQGR.060012* (Vol. 14). US Geological Survey.
- Moschetti, M. P., Churchwell, D., Thompson, E. M., Rekoske, J. M., Wolin, E., & Boyd, O. S. (2021). Seismic wave propagation and basin amplification in the Wasatch front, Utah. *Seismological Research Letters*, 92(6), 3626–3641. <https://doi.org/10.1785/0220200449>
- Olsen, K. B., Pechmann, J. C., & Schuster, G. T. (1996). An analysis of simulated and observed blast records in the Salt Lake Basin. *Bulletin of the Seismological Society of America*, 86(4), 1061–1076. <https://doi.org/10.1785/BSSA0860041061>
- Pan-American Center for Earth and Environmental Studies (PACES). (2012). *Gravity database of the US: Online*. University of Texas, El Paso. Retrieved from <http://research.utep.edu/paces>
- Pang, G., Koper, K. D., Mesimeri, M., Pankow, K. L., Baker, B., Farrell, J., et al. (2020). Seismic analysis of the 2020 Magna, Utah, earthquake sequence: Evidence for a listric Wasatch fault. *Geophysical Research Letters*, 47(18), e2020GL089798. <https://doi.org/10.1029/2020GL089798>
- Pankow, K. L., & Pechmann, J. C. (2005). Determination of low-strain amplification factors in the Salt Lake Valley, Utah, using ANSS data. In W. L. Lund (Ed.), *Proceedings Volume, basin and range Province seismic hazards Summit II* (pp. 253–267). Utah Geological Survey Miscellaneous Publication. Retrieved from https://ugspub.nr.utah.gov/publications/misc_pubs/MP-05-2.pdf
- Pankow, K. L., Rusho, J., Pechmann, J. C., Hale, J. M., Whidden, K., Sumsion, R., et al. (2020). Responding to the 2020 Magna, Utah, earthquake sequence during the COVID-19 pandemic shutdown. *Seismological Research Letters*, 92(1), 6–16. <https://doi.org/10.1785/0220200265>
- Pechmann, J. C., Jensen, K. J., & Magistrale, H. (2010). Constraints on the near surface seismic velocity structure of the Wasatch front region, Utah, from Sonic log analyses. Abstracts of the annual meeting. *Seismological Research Letters*, 81(2), 284–388. <https://doi.org/10.1785/gssrl.81.2.284>
- Petersen, M. D., Shumway, A. M., Powers, P. M., Field, E. H., Moschetti, M. P., Jaiswal, K. S., et al. (2024). The 2023 US 50-state national seismic hazard model: Overview and implications. *Earthquake Spectra*, 40(1), 5–88. <https://doi.org/10.1177/87552930231215428>
- Radkins, H. (1990). Bedrock topography of the Salt Lake Valley, Utah, from constrained inversion of gravity data. In *Master's Thesis*.
- Roten, D., Olsen, K. B., & Pechmann, J. C. (2012). 3-D simulations of M 7 earthquakes on the Wasatch fault, Utah, Part II: Broadband (0–10 Hz) ground motions and nonlinear soil behavior. *Bulletin of the Seismological Society of America*, 102(5), 2008–2030. <https://doi.org/10.1785/0120110286>
- Roten, D., Olsen, K. B., Pechmann, J. C., Cruz-Atienza, V. M., & Magistrale, H. (2011). 3D simulations of M 7 earthquakes on the Wasatch fault, Utah, Part I: Long-period (0–1 Hz) ground motion. *Bulletin of the Seismological Society of America*, 101(5), 2045–2063. <https://doi.org/10.1785/0120110031>
- Sambridge, M. (2014). A Parallel Tempering algorithm for probabilistic sampling and multimodal optimization. *Geophysical Journal International*, 196(1), 357–374. <https://doi.org/10.1093/gji/ggt342>

- Shibutani, T., Ueno, T., & Hirahara, K. (2008). Improvement in the extended-time multitaper receiver function estimation technique. *Bulletin of the Seismological Society of America*, 98(2), 812–816. <https://doi.org/10.1785/0120070226>
- Smith, K., Hardwick, C. L., Kim, H. J., McKean, A. P., Lin, F.-C., van Dam, T., et al. (2023). Mapping Basin geometry with a Novel joint inversion of gravity and seismic data to enhance the Salt Lake Valley, Utah community velocity model. *Geological Society of America Abstracts with Programs*, 55(6), 394786. <https://doi.org/10.1130/abs/2023AM-394786>
- Stephenson, W. J., Williams, R. A., Odum, J. K., & Worley, D. M. (2000). High-resolution seismic reflection surveys and modeling across an area of high damage from the 1994 Northridge earthquake, Sherman Oaks, California. *Bulletin of the Seismological Society of America*, 90(3), 643–654. <https://doi.org/10.1785/0119990112>
- Takeuchi, H., & Saito, M. (1972). Seismic surface waves. In B. A. Bolt (Ed.), *Method in computational physics: Advances in research and applications* (Vol. 11, pp. 217–295). Academic Press. <https://doi.org/10.1016/b978-0-12-460811-5.50010-6>
- Thomson, W. T. (1950). Transmission of elastic waves through a stratified solid medium. *Journal of Applied Physics*, 21(2), 89–93. <https://doi.org/10.1063/1.1699629>
- University of Utah. (1962). University of Utah regional seismic network [Dataset]. *International Federation of Digital Seismograph Networks*. <https://doi.org/10.7914/SN/UU>
- U.S. Geological Survey. (1931). United States national strong-motion network [Dataset]. *International Federation of Digital Seismograph Networks*. <https://doi.org/10.7914/SN/NP>
- U.S. Geological Survey and Utah Geological Survey. (2019). Quaternary fault and fold database for the United States. Retrieved from <https://www.usgs.gov/natural-hazards/earthquake-hazards/faults>
- Wang, N., Roten, D., Olsen, K. B., & Pechmann, J. C. (2017). *Rupture direction, hanging wall, basin, and distance effects on ground motions from large normal-faulting earthquakes, Final Technical Report*. U.S. Geological Survey, Award Nos. G14AP00044 and G14AP00045,44
- Williams, R. A., King, K. W., & Tinsley, J. C. (1993). Site response estimates in Salt Lake Valley, Utah, from borehole seismic velocities. *Bulletin of the Seismological Society of America*, 83(3), 862–889. <https://doi.org/10.1785/BSSA0830030862>
- Wong, I. G., Lund, W. R., DuRoss, C., Thomas, P., Arabasz, W., Crone, A. J., et al. (2016). Earthquake probabilities for the Wasatch front region in Utah, Idaho, and Wyoming. In *Utah Department of natural Resources. Miscellaneous Publication 16-3 Utah Geological Survey*.
- Zeng, Q., & Lin, F.-C. (2023). Groundwater monitoring in Northern Utah (GNU) from one-year nodal deployment [Dataset]. *International Federation of Digital Seismograph Networks. Dataset/Seismic Network*. <https://doi.org/10.7914/sxpj-9z48>
- Zeng, Q., Lin, F.-C., & Allam, A. A. (2022). 3D shear wave velocity model of Salt Lake Valley via Rayleigh wave ellipticity across a temporary geophone array. *The Seismic Record*, 2(2), 127–136. <https://doi.org/10.1785/0320220016>
- Zhang, H., Pankow, K., & Stephenson, W. (2019). A Bayesian Monte Carlo inversion of spatial auto-correlation (SPAC) for near-surface vs structure applied to both broad-band and geophone data. *Geophysical Journal International*, 217(3), 2056–2070. <https://doi.org/10.1093/gji/ggz136>
- Zhu, L., & Kanamori, H. (2000). Moho depth variation in southern California from teleseismic receiver functions. *Journal of Geophysical Research*, 105(B2), 2969–2980. <https://doi.org/10.1029/1999JB900322>